



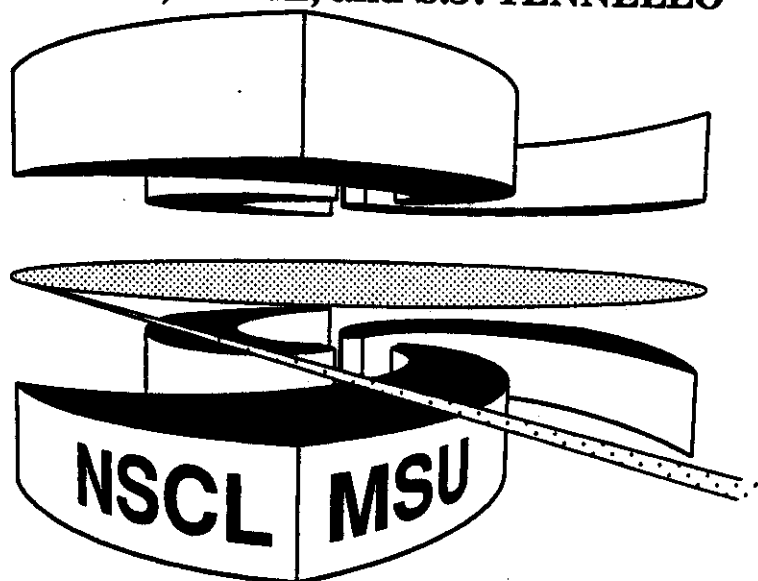
Michigan State University

National Superconducting Cyclotron Laboratory

**IMPACT PARAMETER AND TOTAL MOMENTUM
DEPENDENCE OF TWO-PROTON CORRELATION
FUNCTIONS FOR $^{36}\text{Ar} + ^{45}\text{Sc}$ AT**

E/A = 80 MeV: COMPARISON WITH BUU

**M.A. LISA, C.K. GELBKE, W. BAUER, P. DECOWSKI,
W.G. GONG, E. GUALTIERI, S. HANNUSCHKE,
R. LACEY, T. LI, W. G. LYNCH, C.M. MADER,
G.F. PEASLEE, T. REPOSEUR, A.M. VANDER MOLEN,
G.D. WESTFALL, J. YEE, and S.J. YENNELLO**



Impact Parameter and Total Momentum Dependence of Two-Proton Correlation Functions for $^{36}\text{Ar}+^{45}\text{Sc}$ at $E/A=80$ MeV: Comparison with BUU

M.A. Lisa, C.K. Gelbke, W. Bauer, P. Decowski¹, W.G. Gong²,
E. Gualtieri, S. Hannuschke, R. Lacey³, T. Li, W.G. Lynch,
C.M. Mader, G.F. Peaslee, T. Reposeur⁴, A.M. Vander Molen,
G.D. Westfall, J.Yee, and S.J. Yennello⁵

*National Superconducting Cyclotron Laboratory
Michigan State University, East Lansing, MI 48824, USA*

Abstract

The total momentum dependence of the two-proton correlation function is used to characterize the evolution of the reaction zone created in $^{36}\text{Ar}+^{45}\text{Sc}$ collisions at $E/A=80$ MeV for central and peripheral collisions. Calculations with the Boltzmann-Uehling-Uhlenbeck equation reproduce the measured momentum dependence of the correlation functions well for central collisions. Some disagreement between theory and experiment is observed for peripheral collisions.

PACS number: 25.70.Pq

¹ Present address: Department of Physics, Smith College, Northampton, MA

² Present address: Lawrence Berkeley Laboratory, Berkeley, CA 94720

³ Present address: Department of Chemistry, State University of New York, Stony Brook, NY 11776

⁴ Present address: Laboratoire de Physique Nucléaire, Université de Nantes, Nantes Cedex 03, France

⁵ Present address: Cyclotron Institute, Texas A&M University, College Station, TX 77843

I. INTRODUCTION

Two protons, emitted from the reaction zone created in an energetic heavy ion collision, will mutually interact through the nuclear and Coulomb forces. These interactions, along with the requirement of anti-symmetrization of the two-proton wave function, lead to a distortion of the population of the two-proton phase space as compared to a scenario in which the particles are distinguishable and interactions are not present. The strength of the interaction and hence the amount of distortion, depends on the relative space-time separation of the protons upon emission, as well as on their relative momentum. The two-proton phase space population from a source with a small space-time extent will therefore show large distortion effects due to final-state interactions and quantum statistics. The magnitude of this distortion is measured by the two-proton correlation function, which provides a unique tool for obtaining source sizes [1-7].

The two-proton correlation function has seen extensive use in heavy ion studies aimed at extracting source size and lifetime parameters from the proton-emitting zone [8-29]. Usually, it is evaluated as a function of $q \approx |\mathbf{p}_1 - \mathbf{p}_2|/2$, the magnitude of the momentum of relative motion in the proton pair rest frame. Due to the strongly attractive s-wave interaction between the protons, the two-proton correlation function exhibits a peak at a $q \approx 20$ MeV/c; a more pronounced peak indicates a smaller source size [1].

The dependence of the correlation function on the total momentum of the pair ($P = |\mathbf{p}_1 + \mathbf{p}_2|$) provides valuable information on the evolution of the reaction zone, and may be a method to determine emission and expansion time scales [2-7]. Previous measurements of two-proton correlation functions have found stronger correlations at $q \approx 20$ MeV/c for more energetic protons [19-30], indicating that energetic protons are emitted from smaller sources (or with shorter characteristic timescales) than less energetic protons.

Interpretation of correlation functions is complicated by the lack of a one-to-one relationship between space-time geometry of the source and the correlation function [4]. However, any prediction of reaction zone dynamics unambiguously gives rise to a correlation function and its dependence on P [4]. Therefore, it is valid to require that the P -dependence of the correlation function predicted by a dynamical theory reproduce that seen experimentally.

In previous studies [5,7,19,25,26], two-proton correlation functions predicted by the Boltzmann-Uehling-Uhlenbeck (BUU) transport model were seen to be in good agreement with the total momentum dependence observed in the data. In these comparisons of measured and predicted P -dependences of the correlations, the data lacked a centrality filter, and BUU events were weighted geometrically according to impact parameter and filtered through the detector acceptance.

However, BUU calculations of the total momentum dependence of the correlation function show drastically different behavior for central and

peripheral collisions [5,7]. Comparison of these calculations to data would be interesting; however, without a centrality filter on experimental data, such detailed predictions of the theory have been inaccessible to experimental tests.

In this work, we present the first study of the total momentum dependence of the two-proton correlation function for different regions of centrality and the first experimental test of the reaction zone evolution predicted by the BUU for impact parameter-selected events. Such a double cut on the data requires coincidence statistics not previously available and provides unique information about reaction zone dynamics in central and peripheral collisions.

The work is organized as follows: In the next section, the details of the experimental set-up are discussed. We present an analysis of global observables and their utility in this experiment to select impact parameter in Section III. In Section IV we present the measured correlation functions as a function of total momentum and centrality. The method used to extract correlation functions from the BUU model is briefly discussed in Section V. Comparisons of BUU predictions with the data, using two different methods to weight BUU events, are presented in Section VI. In Section VII we present our conclusions.

II. EXPERIMENTAL SET-UP

From the K-1200 cyclotron at the National Superconducting Cyclotron Laboratory at Michigan State University, a beam of ^{36}Ar ions was extracted and focused onto a ^{45}Sc target of areal density 10.0 mg/cm^2 . Beam intensities as measured by a Faraday cup downstream of the target were typically 3×10^8 beam particles/sec.

The target was located at the center of the MSU 4π array [31]; in this experiment the configuration included the phoswich detectors of the 4π array only. The forward pentagon section of the array consisted of 45 phoswich detectors which covered angles between 7° and 18° with a geometrical efficiency of approximately 56%. The "ball" portion of the MSU 4π array consisted of 164 plastic phoswich detectors, which provided about 85% solid angle coverage at polar angles between 23° and 157° (except for the hexagonal section occupied by the 56-element hodoscope, discussed below). All detectors of the 4π array were read out by photomultiplier tubes, and the "fast" and "slow" components of the phoswich detector signal were digitized by LeCroy FERA ADCs. Timing information was digitized by LeCroy TFC-FERA systems.

Two-dimensional gates in the fast *vs.* slow maps provided particle identification. Particle charge was resolved up to $Z \approx 10$ and mass resolution was obtained for hydrogen isotopes. Energy calibrations of individual phoswich detectors of the 4π array were obtained by matching gains in software to energy spectra with a known calibration; they are accurate to approximately 10%.

Energy thresholds for protons and carbon ions, respectively, were approximately 17 MeV and 380 MeV in ball detectors, and 12 MeV and 260 MeV in the forward array. Because of the fast rise time of the phototubes, random hits from different beam bursts could be easily identified with the use of a one-dimensional time cut.

One of the hexagonal modules of the 4π array centered at 38° was replaced by a 56-element high-resolution hodoscope, described in detail in Refs. [26,32,33]. Angular coverage for this hodoscope is shown in Fig. 1; in this experiment, detectors 27, 47, 49, and 50 did not function. Each element of the hodoscope was a ΔE -E telescope consisting of a planar surface barrier silicon detector (300 μm thickness and 450 mm^2 active area), backed by a 10 cm-long cylindrical CsI(Tl) crystal read out by a PIN diode. Detectors and preamplifiers were temperature stabilized ($T=15^\circ\text{C}$) by cooled alcohol flowing through tubes in copper cooling plates. Gain stability was monitored by pulsers during data-taking. Signals from each component passed through a shaping amplifier with a shaping time of about 3.5 μs , and pulse-heights were digitized by Silena 4418/V peak-sensing ADCs. Timing information relative to cyclotron RF pulses was digitized by LeCroy TFC-FERA systems.

Particle identification was facilitated by the use of a PID function [34] which mapped the ΔE -E space onto a PID-E space in which each hydrogen and helium isotope appears as an easily distinguishable curve with little E-dependence. Calibration of the Si detectors was performed with a precision pulser system which produced linear calibrations for the ΔE -detectors. Energy calibration of the CsI(Tl) detectors for light particles was performed by scattering α beams at $E/A=25, 30,$ and 40 MeV from gold and polypropylene targets. Energy calibrations were linear, and energy resolution was about 1% for 50 MeV protons. Typical energy thresholds for protons were about 8 MeV. Random coincidences in hodoscope detectors were easily identifiable through relative timing spectra after rise-time effects were accounted for off-line.

The majority of the data discussed here was taken with an electronic trigger requiring a two-fold coincidence in the hodoscope. Due to the considerably longer rise time of the hodoscope detectors in relation to the 4π phoswich detectors, a fast-clear circuit was necessary to reject events which triggered the 4π array but not the hodoscope. Events with at least three detectors in the 4π array and two detectors in the hodoscope firing were written on magnetic tape and analyzed off-line. Due to the relatively large polar angle at which the hodoscope was positioned and the relatively high geometric efficiency of the 4π detector array, typical live counting rates were 50,000 events/sec in the 4π detector, 25 of which were in coincidence with two-fold hodoscope events, and therefore were recorded; the remainder were cleared.

Hodoscope singles data were taken in coincidence with the 4π detector with an alternate trigger throughout the run. Inclusive ("minimum bias") 4π data were also acquired via a third trigger.

III. GLOBAL OBSERVABLES USED FOR IMPACT PARAMETER SELECTION

In order to investigate in detail the behaviour of the reaction zone separately for central and peripheral events, cuts on global observables were employed. (All "global" observables discussed here involve sums over particles detected in the 4π array only; particles in the hodoscope are not included in order to avoid effects of "self-cut" biasing in the correlation functions.)

Many dynamical models of nuclear collisions require as an input an impact parameter distribution. When comparing predictions from such models to inclusive data, an obvious choice might be a linear (geometric) weighting of impact parameter up to some cutoff b_{\max} , beyond which the process of interest is assumed to be negligible. Often, however, the experimental detector acceptance biases the data toward a particular impact parameter range. This is particularly true whenever an impact parameter filter is used to place a centrality cut upon the data. When such cuts are applied, one should determine the actual impact parameter distribution sampled by such cuts. Unless the dynamical model provides good agreement with the measured inclusive spectra (after filtering through detector acceptance), a model event calculated for a given impact parameter will have a different probability of passing the cut than will real events produced at the same physical impact parameter. In such cases, the effects of different impact parameter weighting schemes upon the model predictions should be investigated, a task which is often avoided.

In the present analysis, we employ cuts on the total transverse energy E_t , defined by

$$E_t = \sum_i E_i \cdot \sin^2\theta_i, \quad (1)$$

where the index i runs over particles emitted into the energy and angular acceptance of the 4π array.

In Fig. 2, we compare the total transverse energy spectrum dP/dE_t measured with a minimum bias trigger (at least one detector firing) in the 4π detector, and the BUU prediction given a geometric weighting of impact parameter. For the experimental data, the sum in Eq. 1 runs over all charged particles and fragments detected in the 4π array, while for the BUU results, the index is over all emitted nucleons, after passing through detector acceptance. The BUU fails to reproduce the observed E_t spectrum; hence, any comparison with data utilizing centrality cuts based on E_t is suspect. This disagreement is due to the fact that the BUU is a

theory that describes the time evolution of the single particle phase space distribution function and therefore cannot reproduce observables sensitive to the emission of complex fragments. Use of N_C , the total charged particle multiplicity, or Z_y , the midrapidity charge, would also be suspect, since these observables also depend on fragment contributions. This shortcoming of the BUU encourages us to explore two alternative schemes for event selection in the construction of correlation functions.

From the inclusive E_t distributions shown in Fig. 2, it is clear that the use of identical E_t cuts to the experimental data and to the BUU events would be rather meaningless. One may, however, define "equivalent" E_t cuts for BUU events and for measured events. We propose a procedure which assumes that, on average, E_t decreases monotonically with impact parameter and which characterizes both data and BUU events according to where the E_t for the event falls in the respective E_t -distribution. For example, one could assume that the top 10% of the experimental E_t -distribution is produced by the same impact parameters as the top 10% of the theoretical E_t -distribution. In practice, this implies that if dP/dE_t and dP'/dE_t are the total transverse energy probability distributions for the BUU and for the data, respectively, then a cut in the data at E_t corresponds to a cut in the BUU at \hat{E}_t , where the relationship between E_t and \hat{E}_t is given by

$$\int_{\hat{E}_t}^{\infty} dE'_t \cdot \frac{dP'}{dE'_t} = \int_{E_t}^{\infty} dE'_t \cdot \frac{dP}{dE'_t}. \quad (2)$$

A different event-weighting scheme relies upon the extraction of the impact parameter distribution sampled by a set of data. Phair et al. [35] have outlined a technique for constructing an average impact parameter scale based on a global observable, grounded in very general considerations. In this section, we extend the method by giving a prescription for constructing impact parameter distributions that fold in the finite "width," or scale of the fluctuations, in the relationship between impact parameter and the global observable.

An average impact parameter scale can be based upon any global observable, such as E_t , whose average value for a given impact parameter varies monotonically with the impact parameter. The reduced average impact parameter \hat{b} is then defined in terms of this observable X via geometric considerations:

$$\hat{b}(X) = \frac{\langle b(X) \rangle}{b_{\max}} = \sqrt{\int_X^{\infty} dX' \frac{dP}{dX'}}, \quad (3)$$

where b_{\max} is the maximum impact parameter for a collision and dP/dX is the measured inclusive (minimum bias) probability distribution for global observable X .

Plotted in the upper half of Fig. 3 is the measured inclusive total transverse energy distribution, where the total transverse energy of the event is defined in Eq. 1 and the index i runs from 1 to N_C , the charged particle multiplicity detected

in the 4π array. Via Eq. 3, one can use this distribution to deduce the average reduced impact parameter scale, shown in the lower half of the figure.

Through the relationship $\hat{b}(E_t)$, any distribution dP/dE_t can be transformed into an average reduced impact parameter distribution via

$$\frac{dP}{d\hat{b}(E_t)} = \frac{dP}{dE_t} \bigg/ \frac{d\hat{b}(E_t)}{dE_t}. \quad (4)$$

The dashed line in Fig. 4 is the average reduced impact parameter distribution corresponding to a minimum bias trigger. By construction, the minimum bias impact parameter distribution increases linearly with \hat{b} . The solid line shows the corresponding distribution for the set of events in which two protons are measured in the 56-element hodoscope. Clearly this set of events, from which we construct our correlation function, is biased toward central collisions. For comparison, the dot-dashed curve shows the average reduced impact parameter distribution for singles proton data in the hodoscope. This distribution is similar to that for the two proton coincidence events, but displays a somewhat less pronounced shift towards centrality.

Other global observables we have used to construct average reduced impact parameter scales are the charged particle multiplicity N_C and the mid-rapidity charge, Z_Y , where Z_Y is defined as

$$Z_Y = \sum_{i=1}^{N_c} Z_i \cdot \Theta(y_i - 0.75y_{\text{targ}}) \cdot \Theta(0.75y_{\text{proj}} - y_i) \quad (5)$$

with

$$\Theta(x) = \begin{cases} 1 & \text{if } x > 0 \\ 0 & \text{if } x \leq 0 \end{cases} \quad (6)$$

In Eq. 5, and y_{targ} , y_{proj} , and y_i are respectively the rapidity of the target, projectile, and i^{th} charged particle in the center-of-momentum frame of the system.

The quantity $\hat{b}(X)$ is expected to be an approximate measure of the average reduced impact parameter that produces a given value X for a global observable. As such, a sharp cut in the observable X corresponds to a sharp cut in $\hat{b}(X)$. In order to quantify the values of impact parameter that are sampled in a data sample, one must consider the effects of fluctuations in the relationship between impact parameter and global observables.

Following Phair et al., we obtain an estimate of the scale of the fluctuations in the relationship between the true reduced impact parameter \hat{b} and E_t by observing the effect of narrow cuts in $\hat{b}(Z_Y)$ and $\hat{b}(N_C)$ on the distribution

$dP / d\hat{b}(E_t)$. The upper panel of Fig. 5 shows $dP / d\hat{b}(E_t)$ for narrow central cuts in $\hat{b}(N_C)$ (dashed line) and $\hat{b}(Z_Y)$ (dot-dashed line), and for a double-cut on both variables (solid line). Similar distributions are shown in the lower panel for somewhat less central cuts. The widths $\sigma(\hat{b}(E_t))$ of the double-cut distributions can be taken as upper limits of the widths of the distribution of the true reduced impact parameter b_r for a given value of E_t [35]. Similar analyses based on $\hat{b}(N_C)$ and $\hat{b}(Z_Y)$ show slightly larger fluctuations than shown in Fig. 5; hence, we conclude that E_t is a slightly more precise measure of event centrality, in agreement with the analysis of Ref. [35].

To obtain a true reduced impact parameter distribution dP/db_r , it is necessary to fold the effects of the finite widths $\sigma(\hat{b})$ into the impact parameter distribution. As an ansatz, we take the following expression for the probability that an event with global observable corresponding to average reduced impact parameter \hat{b} was in fact the product of a collision with true reduced impact parameter b_r :

$$\frac{dP_{\hat{b}}(b_r)}{db_r} \sim b_r \cdot e^{-(b_r - \hat{b})^2 / 2\sigma(\hat{b})^2} \cdot \Theta(1 - b_r) \cdot \Theta(b_r). \quad (7)$$

For a given cut $E_t^{\min} \leq E_t \leq E_t^{\max}$, the reduced impact parameter distribution can be obtained by incorporating the extracted widths $\sigma(\hat{b})$ as follows:

$$\frac{dP}{db_r} = \int_{\hat{b}(E_t^{\max})}^{\hat{b}(E_t^{\min})} d\hat{b}' \cdot \frac{dP(\hat{b}')}{d\hat{b}'} \cdot \frac{dP_{\hat{b}'}(b_r)}{db_r}. \quad (8)$$

The effect of this smearing is illustrated in Fig. 6. The top panel of the figure shows the E_t -distribution when two protons are found in the hodoscope, and the two cuts we shall denote as "central" and "peripheral." The center panel shows the corresponding cuts on average reduced impact parameter \hat{b} . The solid curves in the bottom panel show the distributions of the true reduced impact parameter b_r deduced from these cuts. The dot-dashed curves in the bottom panel correspond to b_r distributions calculated in a similar fashion for proton singles data; a slightly enhanced probability for larger impact parameters is noted in the singles data.

The solid curves in the bottom panel of Fig. 6 correspond to impact parameter distributions for "central" and "peripheral" events which had two protons in the hodoscope. Hence, these impact parameter distributions have been selected by the application of double gating conditions, and they may not be used as direct input for model calculations. In the construction of input impact parameter distributions for dynamical models, only the centrality cut on $\hat{b}(E_t)$ should be applied; the requirement of particles being detected in the

hodoscope is implicit in the extraction of the correlation function from BUU events (see Section V).

In order to construct impact parameter distributions that may be used as input to dynamical calculations, we construct inclusive distributions dP/db_T for our two centrality cuts. The distribution of impact parameters sampled by these two cuts may then be obtained by inserting the geometric distribution,

$dP/d\hat{b} = 2\hat{b}/\hat{b}_{\max}^2$, into Eq. 8. The upper panel of Fig. 7 shows the sharp cuts in average reduced impact parameter corresponding to our central and peripheral definitions. The solid curves in the lower panel of Fig. 7 show the distributions of true reduced impact parameter deduced from these cuts. These curves may be used to weight events generated by a dynamical model such as the BUU.

Not all events generated by the dynamical model will produce a proton in the hodoscope acceptance. Thus, the impact parameter distributions corresponding to the events that contribute to the correlation function will differ from the "input" impact parameter distributions shown in the lower panel of Fig. 7. We investigate this effect in Fig. 8. The solid curves in the figure show the distributions of impact parameters used to weight our BUU calculations. (The distribution representing the central cut is truncated at very low impact parameters, since we did not run calculations for very small impact parameters for which the geometric cross section is small.) The dotted curves show the corresponding distributions with the additional requirement of proton emission into the direction of the hodoscope. For the peripheral cut, this requirement produces a shift towards smaller impact parameters. The distributions shown by the dotted curves may be compared to those extracted from our data (dashed curves; they are identical to the dotted-dashed curves in Fig. 6). The overall agreement between these two distributions illustrates the quality of the impact parameter selection and reconstruction procedure used in the present analysis.

To summarize this section, we have two possible methods of comparing the data to a model that requires an impact parameter distribution as an input. One may use "equivalent" E_T -cuts on model and data events, or one may extract reduced impact parameter distributions corresponding to a given cut in a global observable. We consider each in section V. Finally, we note that the method of "equivalent" E_T cuts is tantamount to defining a relation $\hat{b}'(E_T^{BUU})$ for BUU events as we have done for the data, and to apply the same cuts on $\hat{b}'(E_T^{BUU})$ and on $\hat{b}(E_T^{\text{exp}})$.

IV. MEASURED TWO-PROTON CORRELATION FUNCTIONS

The two-proton correlation function is obtained by dividing the two-proton coincident yield by a "background" yield which simulates the phase space population of two non-interacting protons. This background yield is constructed by treating as a pair, two protons measured in different singles events. In this

way, the correlation function, usually parameterized in terms of the relative momentum between the proton pair, measures primarily the distortion effects due to the final-state interactions between the protons; single-particle phase space effects largely divide out.

As a check, we have also constructed background yields via the event-mixing technique, in which the background yield is constructed by "mixing" two protons from different coincidence events. Correlation functions constructed using the singles and event-mixing techniques differ on the order of statistical uncertainties, with a slight systematic damping in the correlations observed via the event-mixing technique; this is consistent with previous studies [30]. A large discrepancy between results from the two techniques is not expected, since coincidence and singles data sample very similar ranges of impact parameter (see Fig. 4), especially after gating on total transverse energy of the event (see bottom panel of Fig. 6).

Experimentally, the two-proton correlation function $1+R(q)$ is defined through the relation

$$\sum Y_{12}(\mathbf{p}_1, \mathbf{p}_2) = N(1 + R(q)) \sum Y_1(\mathbf{p}_1) \cdot Y_1(\mathbf{p}_2) \quad (9)$$

where $Y_{12}(\mathbf{p}_1, \mathbf{p}_2)$ is the measured coincidence yield for two protons with momenta \mathbf{p}_1 and \mathbf{p}_2 , and $Y_1(\mathbf{p})$ is the measured singles yield for a proton with momentum \mathbf{p} . The summations are over events selected by the specified gates on E_t and on total momentum $P = |\mathbf{p}_1 + \mathbf{p}_2|$. The correlation function is parameterized in terms of the relative momentum $q = |\mathbf{p}_1 - \mathbf{p}_2| / 2$ of the proton pair, and N is a normalization constant set such that $R(q)=0$ for large q , where final state interactions are believed to be negligible.

Previous studies [9,10,13,17,22] have shown a distinction between correlation functions constructed with central and peripheral events, where centrality is determined by some global observable. At relatively high incident beam energies ($E/A > 50$ MeV), it has been observed [9,10,17] that peripheral events show a more pronounced maximum in the two-proton correlation function at $q \approx 20$ MeV/c than do central events. In this case, a geometric parameterization indicates a smaller emitting source for peripheral events, consistent with a geometric picture of the reaction zone. The opposite trend, however, has been observed in the $^{14}\text{N} + ^{197}\text{Au}$ system at $E/A=35$ MeV. In this latter experiment, measurements were performed at angles sufficiently close to the grazing angle that gates on peripheral events selected large contributions from projectile decays. In this experiment, correlations for peripheral collisions were attenuated as compared to those for central collisions, and this data was interpreted in terms of the lifetime of excited projectile residues and not in terms of a single geometric source size [13,22,36].

In Fig. 9, we display correlation functions corresponding to our centrality cuts (indicated in Figs. 6 and 7) and integrated over pair momentum P . As in

Ref. [17], our measurements of the two-proton correlation function are performed at angles far back of the grazing angle where contributions from projectile decays are small, and our results are qualitatively consistent with the trends previously observed at higher beam energies.

In Fig. 10, the two-proton correlation function is shown for cuts on the total momentum of the proton pair. For the slowest protons ($P=400-520$ MeV/c), the peripheral data show an enhanced correlation at $q \approx 20$ MeV/c relative to the central data, indicating a smaller implied source size for peripheral collisions. For the fastest protons ($P \geq 880$ MeV/c), however, the height of the bump at $q \approx 20$ MeV/c is quite similar for central and peripheral cuts.

These trends are summarized in Fig. 11, where the average value of the correlation function in the region $q=15-25$ MeV/c, $\langle 1+R \rangle_{15-25 \text{ MeV/c}}$ is plotted against the total momentum of the proton pair for the two centrality cuts. Error bars indicate statistical uncertainties as well as an estimate of the uncertainty due to normalization in the high- q region. For orientation, the right scale gives the radius parameters r_0 calculated in the Koonin formalism [1] for zero-lifetime spherical sources of Gaussian density profile, $\rho(r) \propto \exp(-r^2/r_0^2)$, which predict the values of $\langle 1+R \rangle_{15-25 \text{ MeV/c}}$ shown on the left.

Correlation functions from central and peripheral collisions display distinct dependences on the total momentum P of the proton pair. A decreasing source size for increasing P is indicated for both regions of centrality, with a stronger dependence seen for central collisions. This may indicate that the effect of source expansion is more prominent in central collisions.

V. EXTRACTION OF CORRELATION FUNCTIONS FROM BUU EVENTS

In this work, we use the BUU model of Bauer [7,37-40] with a stiff equation of state ($K = 380$ MeV) and the nucleon-nucleon cross section set to its free value. The BUU transport equation was solved via the test particle method [41], in which many ensembles (or "events") for a given set of initial conditions are run simultaneously. To simulate a geometric distribution of impact parameters, the number of ensembles at a given impact parameter b was set to $N_b = 130 \cdot b$, where b has units of fm. Impact parameters between 1 and 10 fm were run in 0.5 fm steps. In this way, one obtains an ensemble of BUU events representing a geometric distribution of impact parameters. "Central" and "peripheral" subsets of events are chosen from this ensemble according to the methods described in Section III and below.

The phase-space population distribution was evolved by the BUU in steps of 0.5 fm/c on a spatial grid of dimensions $81 \times 81 \times 161$ fm³. An unambiguous indication of when and where a particle is emitted is not provided by the BUU; we employed emission criteria similar to those used previously [5,7,19,25,26]: a

proton was considered "emitted" if it found itself in a region of local matter density eight times less than that of normal nuclear matter before a time $t_{\max}=150$ fm/c. Following the formalism of Refs. 4 and 5, these sets of phase space points can be used to construct correlation functions.

We denote the set of phase space points as $(\mathbf{x}, \mathbf{p})_{ib}^n$, where \mathbf{b} is the impact parameter vector. The event number n runs from 1 to $N_{\mathbf{b}}$, where $N_{\mathbf{b}}$ denotes the number of events with impact parameter vector \mathbf{b} . Finally, i is the particle number in the event (n, \mathbf{b}) ; $i=1 \dots M_{n, \mathbf{b}}$, where $M_{n, \mathbf{b}}$ is the multiplicity of event (n, \mathbf{b}) . Then, the correlation function is calculated as

$$1 + R(q) = \frac{C \sum_{\mathbf{b}} \frac{1}{N_{\mathbf{b}}} \sum_{n_1}^{N_{\mathbf{b}}} \sum_{n_2}^{N_{\mathbf{b}}} \sum_i^{M_{n_1, \mathbf{b}}} \sum_j^{M_{n_2, \mathbf{b}}} (1 - \delta_{ij} \delta_{n_1, n_2}) \delta_{\Delta} \left(q - \frac{|\mathbf{p}_{ib_1}^{\prime n_1} - \mathbf{p}_{jb_2}^{\prime n_2}|}{2} \right) \left| \Phi \left(\mathbf{x}_{ib_1}^{\prime n_1} - \mathbf{x}_{jb_2}^{\prime n_2}; \frac{|\mathbf{p}_{ib_1}^{\prime n_1} - \mathbf{p}_{jb_2}^{\prime n_2}|}{2} \right) \right|^2}{\sum_{\mathbf{b}_1} \sum_{\mathbf{b}_2} \sum_{n_1}^{N_{\mathbf{b}_1}} \sum_{n_2}^{N_{\mathbf{b}_2}} \sum_i^{M_{n_1, \mathbf{b}_1}} \sum_j^{M_{n_2, \mathbf{b}_2}} (1 - \delta_{ij} \delta_{n_1, n_2} \delta_{\mathbf{b}_1, \mathbf{b}_2}) \delta_{\Delta} \left(q - \frac{|\mathbf{p}_{ib_1}^{\prime n_1} - \mathbf{p}_{jb_2}^{\prime n_2}|}{2} \right)} \quad (10)$$

Here, the primed momenta are calculated in the center-of-momentum frame of the proton pair and the double-primed coordinates are calculated in the center-of-momentum frame at the time of emission of the second particle; Φ is the wavefunction of relative motion between the two protons; $\delta_{\Delta}(q)$ is the "binning function" which is unity for $|q| \leq \frac{1}{2} \Delta$ and zero otherwise; C is a constant adjusted such that $R(q)$ vanishes for large q .

Construction of correlation functions with the "equivalent" E_t technique is performed by setting $N_{\mathbf{b}}$ proportional to $|\mathbf{b}|$, consistent with a geometric weighting of impact parameters. The sums in Eq. 10 are then required to include only those events that have a total transverse energy that fall within the desired cut.

Construction of the correlation function according to the experimentally determined impact parameter distributions is performed by setting $N_{\mathbf{b}}$ proportional to the distributions $dP/d|\mathbf{b}|$ shown in the bottom panel of Fig. 7.

VI. COMPARISON OF DATA WITH BUU PREDICTIONS

As demonstrated above, a set of data with a sharp cut in a global observable is actually associated with a smooth distribution of impact parameters. Central and peripheral cuts, employed in our analysis via high or low values of E_t , imply the reduced impact parameter distributions shown in Fig. 7. Using these curves as weighting functions, we may randomly choose BUU events based on impact parameter. Correlation functions derived from the central and peripheral sets of BUU events chosen in this way are compared to the data in Fig. 12. Good

agreement between model predictions and observed correlation functions as a function of total pair momentum $P = |\mathbf{p}_1 + \mathbf{p}_2|$ is seen for central events, while the prediction for fast (high P) proton pairs from peripheral events disagrees with the data.

The dependence of the correlation function on total momentum is again summarized in Fig. 13 where the height of the correlation function at $q \approx 20$ MeV/c is plotted against P , for central (upper panel) and peripheral (lower panel) events. Predictions of the BUU model with the impact parameter distributions indicated in Fig. 7 are shown as open circles connected by dashed lines, and are labeled " \hat{b} -selected." The total momentum dependence of the correlation function for central events, shown in the upper panel, is seen to be well reproduced, while that for peripheral events disagrees significantly with measurement.

The heights of correlation functions constructed from sets of BUU events which satisfy "equivalent- E_t " cuts, as described above, are shown in Fig. 13 as the open squares labeled " E_t -selected." The "equivalent- E_t " impact parameter selection procedure leads to final predictions which are practically equivalent to those obtained via the more elaborate \hat{b} -selection procedure.

VII. CONCLUSIONS

This work represents the first study of two-proton correlation functions with double cuts on impact parameter and total momentum of the pair. We observe a different dependence of the correlation function on the total momentum for central and peripheral events, indicating a distinct evolution of the reaction zone for these two classes of events. In particular, the total momentum dependence of the source size, as indicated by the height of the correlation function for $q \approx 20$ MeV/c, is observed to be stronger for central than for peripheral events; this may indicate that expansion effects are more important for central collisions.

The centrality of an experimental event was determined from E_t . However, the E_t distribution produced by the BUU model, given a geometric impact parameter distribution and filtered through detector acceptance, fails to reproduce the E_t distribution measured with a minimum bias trigger; therefore, comparing data to BUU events selected using the same cut in E_t is meaningless. Two alternative methods of selecting BUU events for comparison were employed. In one, "equivalent- E_t " cuts were applied to experimental and BUU events. In the other, "experimental" impact parameter distributions were used as inputs to the BUU. These distributions were obtained by an extension of the geometric method of Phair et al., in which fluctuations in the relationship between impact parameter and E_t are approximately accounted for.

Both methods give approximately the same results. For central collisions, the BUU describes the total momentum dependence of the correlation function quite

well. It is then reasonable to assume that the space-time evolution of the proton-emitting zone generated in central collisions is also fairly well described by the theory. However, the theoretical calculations fail to reproduce the total momentum dependence of the correlation function for peripheral events. Although both schemes employed in the comparison of experimental and model results provided consistent results, one cannot rule out the possibility that the disagreement between experimental and theoretical results for peripheral collisions could still result from a poor understanding of the impact parameter filters employed in this measurement. Some additional theoretical uncertainties exist, due to ambiguities in the criteria for where and when a particle is emitted. (In this work, we have employed a previously used local-density criterion.) Finally, the discrepancies for peripheral collisions may indicate that the present model is incomplete in its description of peripheral collisions and that it may be deficient in its description of surface effects. If so, the utility of the BUU in its present formulation may be limited to the description of central collisions. In any event, care should be taken to choose appropriate impact parameter distributions for input to the model.

ACKNOWLEDGMENTS

The authors would like to thank Scott Pratt for helpful discussions and suggestions concerning the construction of the correlation functions. This work was supported by the National Science Foundation under Grants No. PHY-8913815, PHY-9017077, and PHY-9214992. One of us (W.B.) acknowledges support from a NSF Presidential Faculty Fellow Award.

References

1. S.E. Koonin, *Phys. Lett.* **70B**, 43 (1977).
2. D.H. Boal and J.C. Shillcock, *Phys. Rev.* **C33**, 549 (1986).
3. D.H. Boal and H. DeGuise, *Phys. Rev. Lett.* **57**, 2901 (1986).
4. S. Pratt and M.B. Tsang, *Phys. Rev.* **C36**, 2390 (1987).
5. W.G. Gong, W. Bauer, C.K. Gelbke, and S. Pratt, *Phys. Rev.* **C43**, 781 (1991).
6. D.H. Boal, C.K. Gelbke, and B.K. Jennings, *Rev. Mod. Phys.* **62**, 553 (1990).
7. W. Bauer, C.K. Gelbke, and S. Pratt, *Ann. Rev. Nucl. Part. Sci.* **42**, 77 (1992).
8. F. Zarbaksh, A.L. Sagle, F. Brochard, T.A. Mulera, V. Perez-Mendez, R. Talaga, I. Tanihata, J.B. Carroll, K.S. Ganezer, G. Igo, J. Oostens, D. Woodard, and R. Sutter, *Phys. Rev. Lett.* **46** 1268 (1981).
9. A. Kyanowski, F. Saint-Laurent, D. Ardouin, H. Delagrangé, H. Doubre, C. Grégoire, W. Mittig, A. Péghaire, J. Péter, Y.P. Viyogi, B. Zwieglinski, J. Québert, G. Bizard, F. Lefèbvres, B. Tamain, J. Pochodzalla, C.K. Gelbke, W. Lynch, and M. Maier, *Phys. Lett.* **B181**, 43 (1986).
10. H.A. Gustafsson, H.H. Gutbrod, B. Kolb, H. Loehner, B. Ludewigt, A.M. Poskanzer, T. Renner, H. Riedesel, H.G. Ritter, A. Warwick, F. Weik, and H. Wieman, *Phys. Rev. Lett.* **53**, 544 (1984).
11. C.B. Chitwood, J. Aichelin, D.H. Boal, G. Bertsch, D.J. Fields, C.K. Gelbke, W.G. Lynch, M.B. Tsang, J.C. Shillcock, T.C. Awes, R.L. Ferguson, F.E. Obenshain, F. Plasil, R.L. Robinson, and G.R. Young, *Phys. Rev. Lett.* **54**, 302 (1985).
12. B. Erasmus, N. Carjan, and D. Ardouin, *Phys. Rev.* **C44**, 2663 (1991).
13. Z. Chen, C.K. Gelbke, J. Pochodzalla, C.B. Chitwood, D.J. Fields, W.G. Lynch, and M.B. Tsang, *Phys. Lett.* **B186**, 280 (1987).
14. D. Ardouin, F. Lautrido, D. Durand, D. Goujdami, F. Guilbault, C. Lebrun, A. Péghaire, J. Québert, and F. Saint-Laurent, *Nucl. Phys.* **A495**, 57c (1989).
15. P.A. DeYoung, C.J. Gelderloos, D. Kortering, J. Sarafa, K. Zienert, M.S. Gordon, B.J. Fineman, G.P. Gilfoyle, X. Lu, R.L. McGrath, D.M. de Castro Rizzo, J.M. Alexander, G. Auger, S. Kox, L.C. Vaz, C. Beck, D.J. Henderson, D.G. Kovar, and M.F. Vineyard, *Phys. Rev.* **C41**, R1885 (1990).
16. P.A. DeYoung, M.S. Gordon, Xiu qin Lu, R.L. McGrath, J.M. Alexander, D.M. de Castro Rizzo, and L.C. Vaz, *Phys. Rev.* **C39**, 128 (1989).
17. P. Dupieux, J.P. Alard, J. Augerat, R. Babinet, N. Bastid, F. Brochard, P. Charmensat, N. De Marco, H. Fanet, Z. Fodor, L. Fraysse, J. Girard, P. Gorodetzky, J. Gosset, C. Laspalles, M.C. Lemaire, D. L'Hôte, B. Lucas, J. Marroncle, G. Montarou, M.J. Parizet, J. Poitou, D. Qassoud, C. Racca, A. Rahmani, W. Schimmerling, and O. Vallete, *Phys. Lett.* **B200**, 17 (1988).

18. D. Fox, D.A. Cebra, J. Karn, C. Parks, A. Pradhan, A. Vander Molen, J. van der Plicht, G.D. Westfall, W.K. Wilson, and R.S. Tickle, *Phys. Rev.* **C38**, 146 (1988).
19. F. Zhu, W.G. Lynch, T. Murakami, C.K. Gelbke, Y.D. Kim, T.K. Nayak, R. Pelak, M.B. Tsang, H.M. Xu, W.G. Gong, W. Bauer, K. Kwiatkowski, R. PJaneta, S. Rose, V.E. Viola, Jr., L.W. Woo, S. Yennello, and J. Zhang, *Phys. Rev.* **C44**, R582 (1991).
20. T.C. Awes, R.L. Ferguson, F.E. Obenshain, F. Plasil, G.R. Young, S. Pratt, Z. Chen, C.K. Gelbke, W.G. Lynch, J. Pochodzalla, H.M. Xu, *Phys. Rev. Lett.* **61**, (1988).
21. Z. Chen, C.K. Gelbke, W.G. Gong, Y.D. Kim, W.G. Lynch, M.R. Maier, J. Pochodzalla, M.B. Tsang, F. Saint-Laurent, D. Ardouin, H. Delegrange, H. Doubre, J. Kasagi, A. Kyanowski, A. Péghaire, J. Péter, E. Rosato, G. Bizard, F. Lefèbvres, B. Tamain, J. Québert, Y.P. Viyogi, *Phys. Rev.* **C36**, 2297 (1987).
22. Z. Chen, C.K. Gelbke, J. Pochodzalla, C.B. Chitwood, D.J. Fields, W.G. Gong, W.G. Lynch, and M.B. Tsang, *Nucl. Phys.* **A473**, 564 (1987).
23. J. Pochodzalla, C.K. Gelbke, W.G. Lynch, M. Maier, D. Ardouin, H. Delagrange, H. Doubre, C. Grégoire, A. Kyanowski, W. Mittag, A. Péghaire, J. Péter, F. Saint-Laurent, B. Zwieglinski, G. Bizard, F. Lefèbvres, B. Tamain, J. Québert, Y.P. Viyogi, W.A. Friedman, and D.H. Boal, *Phys. Rev.* **C35**, 1695 (1987).
24. W.G. Gong, C.K. Gelbke, N. Carlin, R.T. de Souza, Y.D. Kim, W.G. Lynch, T. Murakami, G. Poggi, D. Sanderson, M.B. Tsang, H.M. Xu, D.E. Fields, K. Kwiatkowski, R. PJaneta, V.E. Viola, Jr., S.J. Yennello, and S. Pratt, *Phys. Lett.* **B246**, 21 (1990).
25. W.G. Gong, W. Bauer, C.K. Gelbke, N. Carlin, R.T. de Souza, Y.D. Kim, W.G. Lynch, T. Murakami, G. Poggi, D. Sanderson, M.B. Tsang, H.M. Xu, S. Pratt, D.E. Fields, K. Kwiatkowski, R. PJaneta, V.E. Viola, Jr., and S.J. Yennello, *Phys. Rev. Lett.* **65**, 2114 (1990).
26. W.G. Gong, C.K. Gelbke, W. Bauer, N. Carlin, R.T. de Souza, Y.D. Kim, W.G. Lynch, T. Murakami, G. Poggi, D. Sanderson, M.B. Tsang, H.M. Xu, D.E. Fields, K. Kwiatkowski, R. PJaneta, V.E. Viola, Jr., S.J. Yennello, and S. Pratt, *Phys. Rev.* **C43**, 1804 (1991).
27. J. Pochodzalla, C.B. Chitwood, D.J. Fields, C.K. Gelbke, W.G. Lynch, M.B. Tsang, D.H. Boal, and J.C. Shillcock, *Phys. Lett.* **B174**, 36 (1986).
28. W.G. Lynch, C.B. Chitwood, M.B. Tsang, D.J. Fields, D.R. Klesch, C.K. Gelbke, G.R. Young, T.C. Awes, R.L. Ferguson, F.E. Obenshain, F. Plasil, R.L. Robinson, and A.D. Panagiotou, *Phys. Rev. Lett.* **51**, 1850 (1983).
29. D. Goujdami, F. Guilbault, C. Lebrun, D. Ardouin, H. Dabrowski, S. Pratt, P. Lautridou, R. Boisgard, J. Québert, and A. Péghaire, *Z. Phys.* **A339**, 293 (1991).

30. M.A. Lisa, W.G. Gong, C.K. Gelbke, and W.G. Lynch, *Phys. Rev.* **C44**, 2865 (1991).
31. G.D. Westfall, J.E. Yurkon, J. van der Plicht, Z.M. Koenig, B.V. Jacak, R. Fox, G.M. Crawley, M.R. Maier, and B.E. Hasselquist, *Nucl. Instr. and Meth.* **A238**, 347 (1985).
32. W.G. Gong, Y.D. Kim, G. Poggi, Z. Chen, C.K. Gelbke, W.G. Lynch, M.R. Maier, T. Murakami, M.B. Tsang, H.M. Xu, and K. Kwiatkowski, *Nucl. Instr. and Meth.* **A268**, 190 (1988).
33. W.G. Gong, N. Carlin, C.K. Gelbke, and R. Dayton, *Nucl. Instr. and Meth.* **A287**, 639 (1990).
34. T. Shimoda, M. Ishihara, and K. Nagatani, *Nucl. Instr. and Meth.* **165**, 261 (1979).
35. L. Phair, D.R. Bowman, C.K. Gelbke, W.G. Gong, Y.D. Kim, M.A. Lisa, W.G. Lynch, G.F. Peaslee, R.T. de Souza, M.B. Tsang, and F. Zhu, *Nucl. Phys.* **A548**, 489 (1992).
36. W.G. Lynch, C.B. Chitwood, M.B. Tsang, D.J. Fields, D.R. Klesch, C.K. Gelbke, G.R. Young, T.C. Awes, R.L. Ferguson, F.E. Obenshain, F. Plasil, R.L. Robinson, and A.D. Panagiotou, *Phys. Rev. Lett.* **52**, 2302 (1984).
37. W. Bauer, G.F. Bertsch, W. Cassing, and U. Mosel, *Phys. Rev.* **C34**, 2127 (1986).
38. W. Bauer, *Nucl. Phys.* **A471**, 604 (1987).
39. B.A. Li and W. Bauer, *Phys. Rev.* **C44**, 450 (1991).
40. B.A. Li, W. Bauer, and G.F. Bertsch, *Phys. Rev.* **C44**, 2095 (1991).
41. G.F. Bertsch, H. Kruse, and S. Das Gupta, *Phys. Rev.* **C29**, 673 (1984).

Figure Captions

Figure 1 Angular coverage of the 56-element high-resolution hodoscope. Each telescope covered about 0.37 msr in solid angle.

Figure 2 Total transverse energy spectrum dP/dE_t measured under a minimum bias trigger in the 4π array is shown as the solid line. Total transverse energy for the event is defined as $E_t = \sum_i E_i \sin^2 \theta_i$, where the sum runs over all detected fragments in the event. Also plotted is the prediction of the BUU model, after passing through the detector acceptance of the 4π array. The dashed and dot-dashed lines indicate calculations in which the definition of E_t includes contributions from all emitted nucleons, and from protons only, respectively. Relative normalization gives equal area for all spectra in the region $E > 100$ MeV.

Figure 3 Plotted in the upper panel is the measured transverse energy distribution dP/dE_t under a minimum bias trigger. The lower panel shows the average reduced impact parameter scale that is based on this distribution.

Figure 4 Plotted are average reduced impact parameter distributions based upon the total transverse energy distributions as discussed in the text. The dashed line indicates the distribution for events taken under a minimum bias trigger; the geometric weighting of impact parameters is a natural consequence of our impact parameter scaling scheme. The solid line shows the average reduced impact parameter for events which have two protons in the 56-element hodoscope. This set of events, which is used to construct two-proton correlation functions, shows a bias toward low impact parameters. The distribution corresponding to proton singles events is shown by the dot-dashed curve; a somewhat less pronounced bias towards centrality is seen for these events.

Figure 5 Average reduced impact parameter distributions $dP/d\hat{b}(E_t)$ for narrow cuts on average reduced impact parameters deduced from other global observables. The specific cuts imposed are indicated in the figure. The dot-dashed curves indicate $dP/d\hat{b}(E_t)$ for events passing through narrow cuts in $\hat{b}(Z_Y)$, where Z_Y is the midrapidity charge. Dashed curves show $dP/d\hat{b}(E_t)$ for a narrow cut in $\hat{b}(N_C)$, where N_C is the total charged particle multiplicity. Solid lines indicate a double-cut involving both variables. The upper panel shows $dP/d\hat{b}(E_t)$ for central cuts on $\hat{b}(X)$, and the lower for mid-central cuts.

Figure 6 Top Panel: Total transverse energy distribution dP/dE_t for events which have two protons in the hodoscope. The cuts we define as "central" (high E_t) and "peripheral" (low E_t) are indicated by the shaded regions .

Center Panel: The average reduced impact parameter distribution $dP/d\hat{b}(E_t)$ corresponding to the total transverse energy distribution of the top panel. Centrality cuts corresponding to those shown in the top panel are indicated by similar shading.

Bottom Panel: Reduced impact parameter distributions dP/db_r corresponding to the centrality cuts shown in the upper two panels. Note that although the cuts on the data are disjunct in E_t , and, therefore in $\hat{b}(E_t)$, the true impact parameter distributions for the two cuts overlap somewhat. Solid lines indicate reduced impact parameter distributions for two-proton coincidence events, while dot-dashed lines represent similar distributions for singles proton events.

Figure 7 Upper Panel: Sharp average reduced impact parameter cuts corresponding to the definition of central and peripheral events are indicated for a geometric distribution of impact parameter.

Lower Panel: Reduced impact parameter distributions dP/db_r corresponding to the centrality cuts indicated above are plotted.

Figure 8 Comparison of experimentally reconstructed impact parameter distributions to those used in the BUU calculations. Solid curves show the impact parameter distribution used to weight BUU events. This distribution is modified by the additional requirement of proton emission towards the hodoscope (dotted curves). The dashed curves show the experimental reduced impact parameter distribution (see Eqs. 4, 7, and 8) when a proton is detected in the hodoscope (same as dotted-dashed curve in Fig. 6).

Figure 9 Energy-integrated two-proton correlation functions measured in the 56-element hodoscope for the centrality cuts indicated in Figure 6. Central events (high E_t) are indicated by solid points, and peripheral events (low E_t) by open points. Statistical errors are smaller than the symbol size.

Figure 10 Measured two-proton correlation functions for a double cut on the total momentum of the pair $P = |\mathbf{p}_1 + \mathbf{p}_2|$ and the impact parameter; centrality cuts are indicated in Figure 6. Open and solid points indicate peripheral and central events, respectively. The upper panel shows the correlation function for slow protons, $400 \text{ MeV}/c \leq P \leq 520 \text{ MeV}/c$. The lower panel shows the correlation function for fast protons, $P \geq 880 \text{ MeV}/c$. Statistical errors are indicated when they are larger than the symbol size.

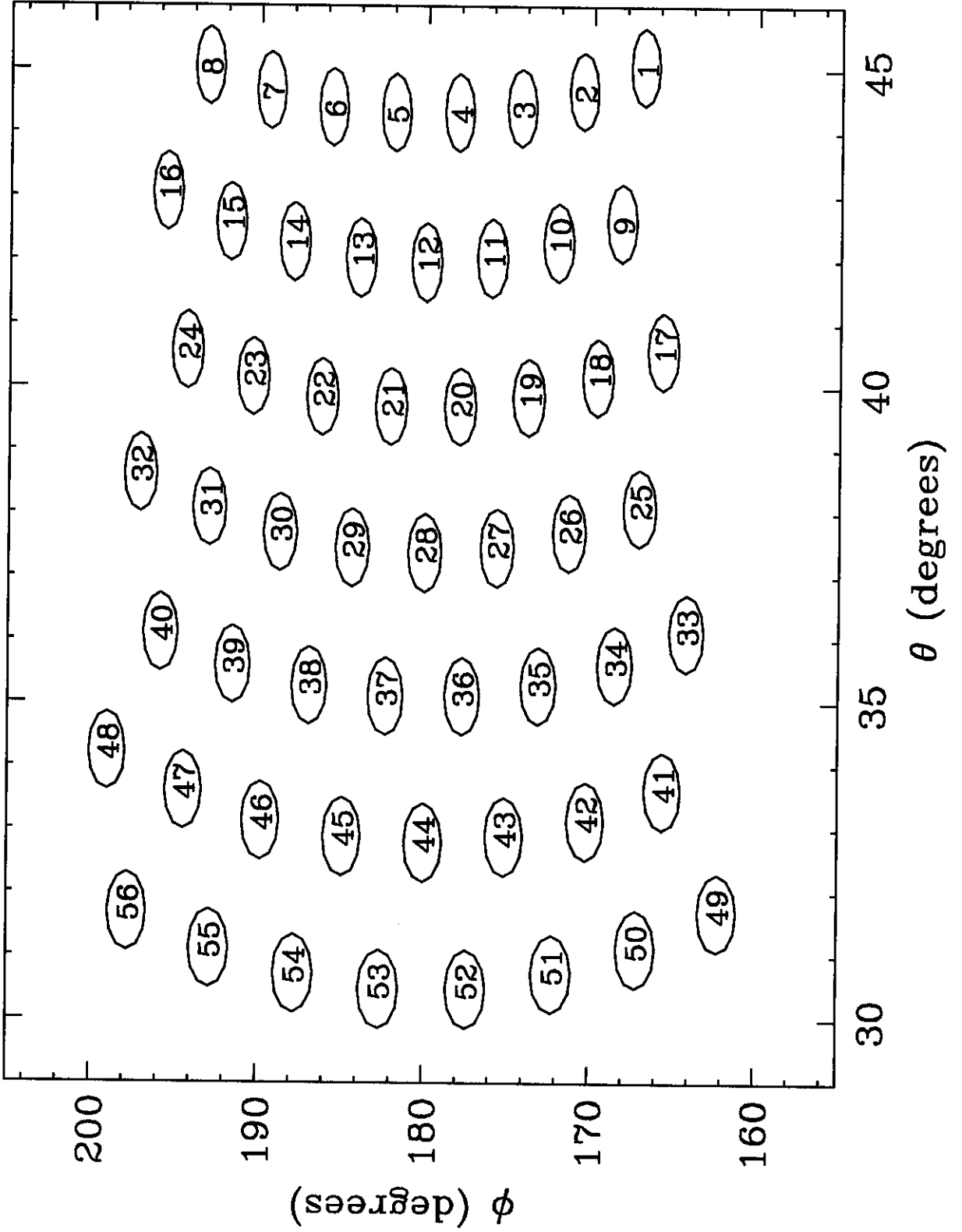
Figure 11 The total momentum dependence of the correlation function is summarized by plotting the height of the correlation in the region $15 \text{ MeV}/c \leq q \leq 25 \text{ MeV}/c$ as a function of the total momentum P . For reference, on the right-hand axis is indicated the radius of a zero-lifetime spherical source of Gaussian density profile that would produce a correlation of equal magnitude. Solid lines which connect the points for central and peripheral events are drawn to guide the eye. Error bars indicate statistical errors in the region $15 \text{ MeV}/c \leq q \leq 25 \text{ MeV}/c$ as well as uncertainties in the height due to uncertainties in normalizing the data at large relative momentum.

Figure 12 Measured two-proton correlation functions for cuts in centrality and total momentum are compared to BUU predictions. Solid symbols represent data; open symbols are BUU calculations. The upper panels show the correlation

function for slow protons ($400 \text{ MeV}/c \leq P \leq 520 \text{ MeV}/c$); lower panels correspond to faster protons ($P \geq 880 \text{ MeV}/c$). Panels on the left- and right-hand sides, respectively, correspond to central and peripheral events. Centrality cuts for the data were based on E_t as indicated by Figure 6. Weighting for BUU events was done according to the reduced impact parameter distributions dP/db_r indicated in the bottom panel of Figure 6. Statistical uncertainties are indicated when they are larger than the size of the points.

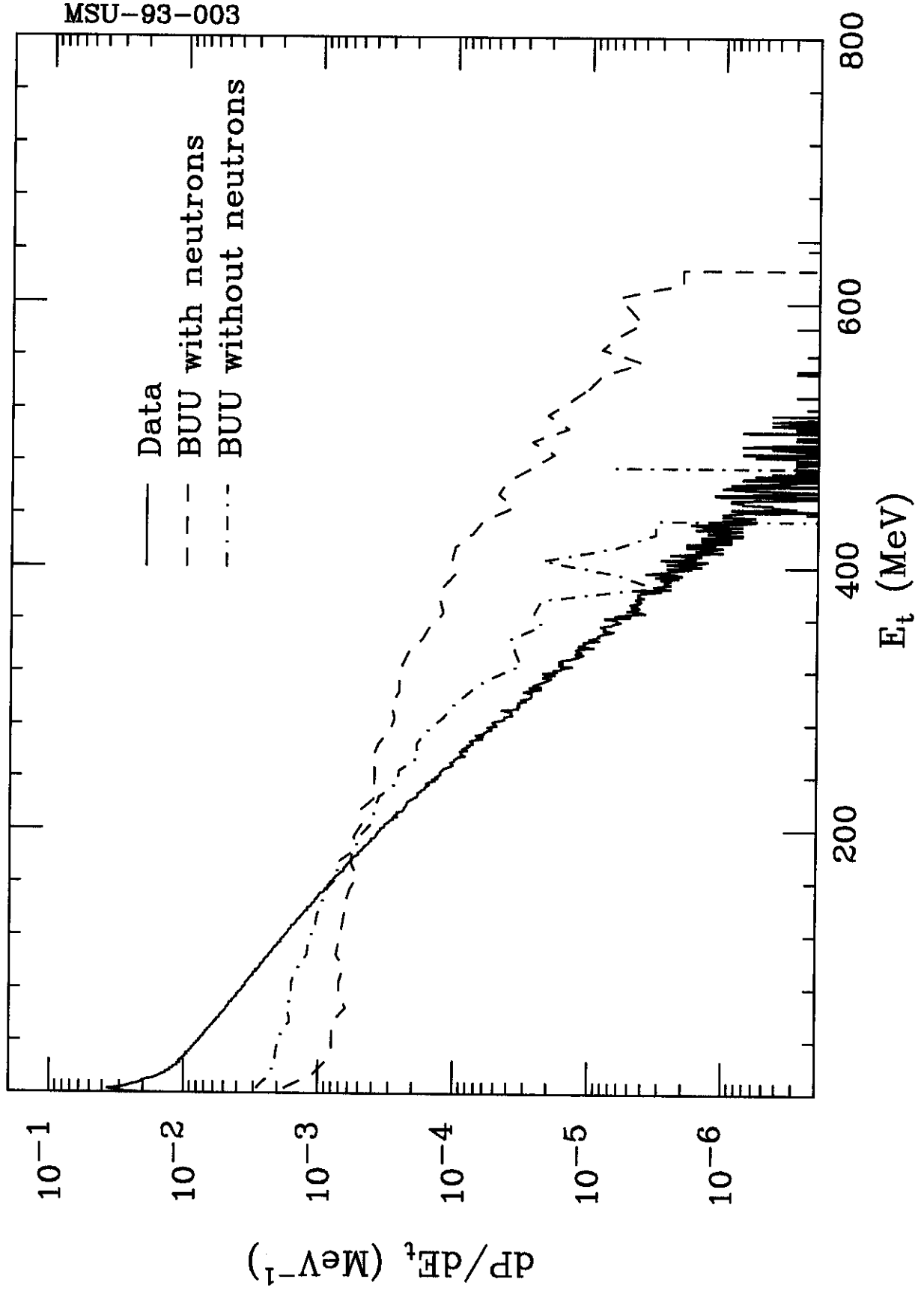
Figure 13 The average height of the correlation function in the region $15 \text{ MeV}/c \leq q \leq 25 \text{ MeV}/c$, is plotted against the total momentum of the pair P . For orientation, the right-hand axis indicates the source radius of a zero- lifetime spherical source with a Gaussian density profile that would produce a correlation of equal magnitude. The upper panel displays the data and calculations for central events, and the lower panel provides the comparison for peripheral events. Data are indicated by solid circles, while BUU predictions are indicated by the open symbols. The open circles correspond to BUU results when the event selection is performed according to the dP/db_r distributions shown in the bottom panel of Figure 6. The open squares correspond to the selection of events via the "equivalent- E_t " method discussed in the text. The lines which connect the data points and BUU predictions are drawn to guide the eye. Error bars on the data points include both statistical errors in the region $15 \text{ MeV}/c \leq q \leq 25 \text{ MeV}/c$ as well as the uncertainties in normalizing the correlation function at large relative momentum. Error bars on BUU predictions were obtained by comparing the variations between predictions for $\langle 1+R \rangle_{15-25 \text{ MeV}/c}$ from three independent ensembles of events chosen via the E_t or \hat{b} methods.

56-element Hodoscope Acceptance



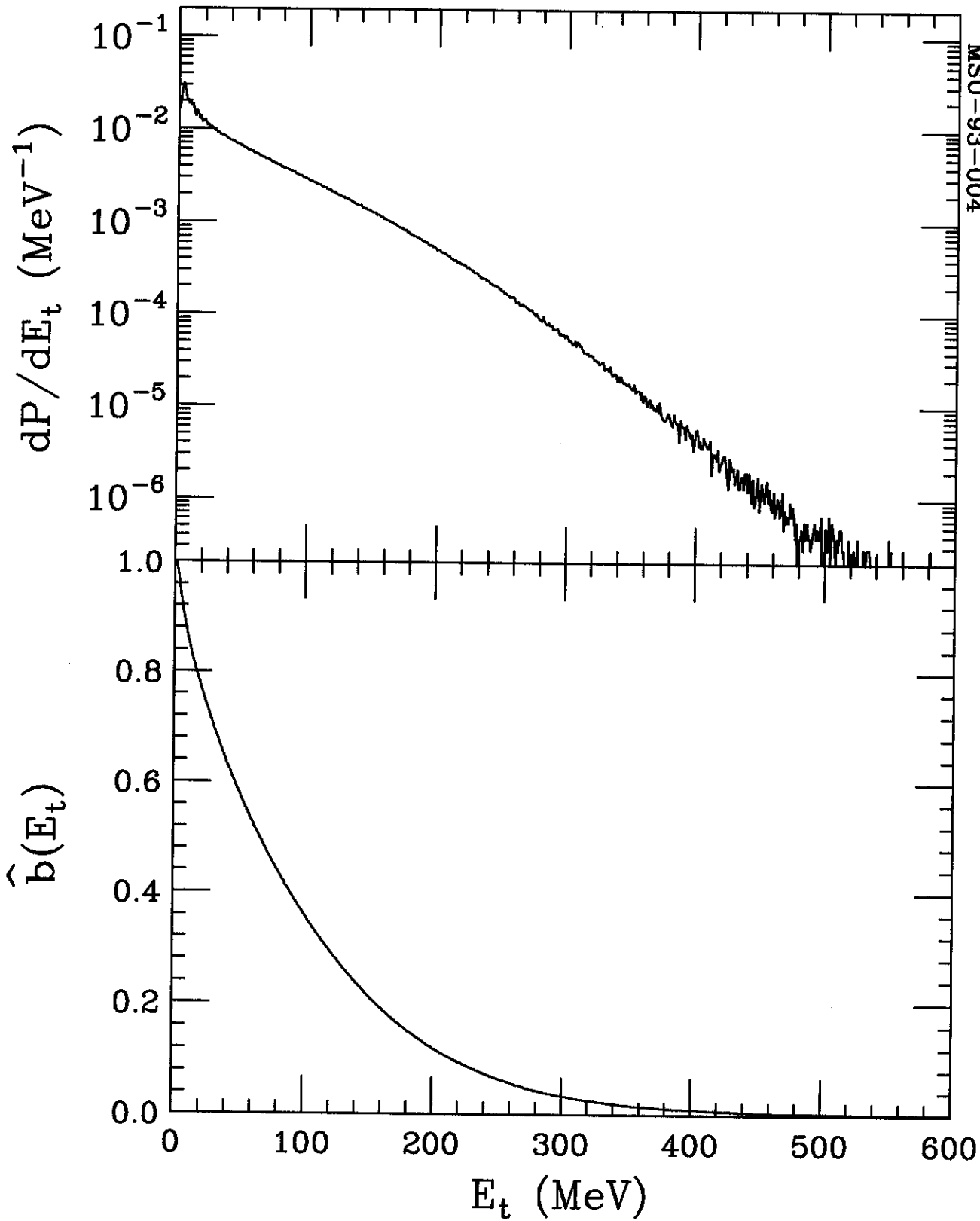
$^{36}\text{Ar} + ^{45}\text{Sc}; E/A=80\text{MeV}$

MSU-93-003



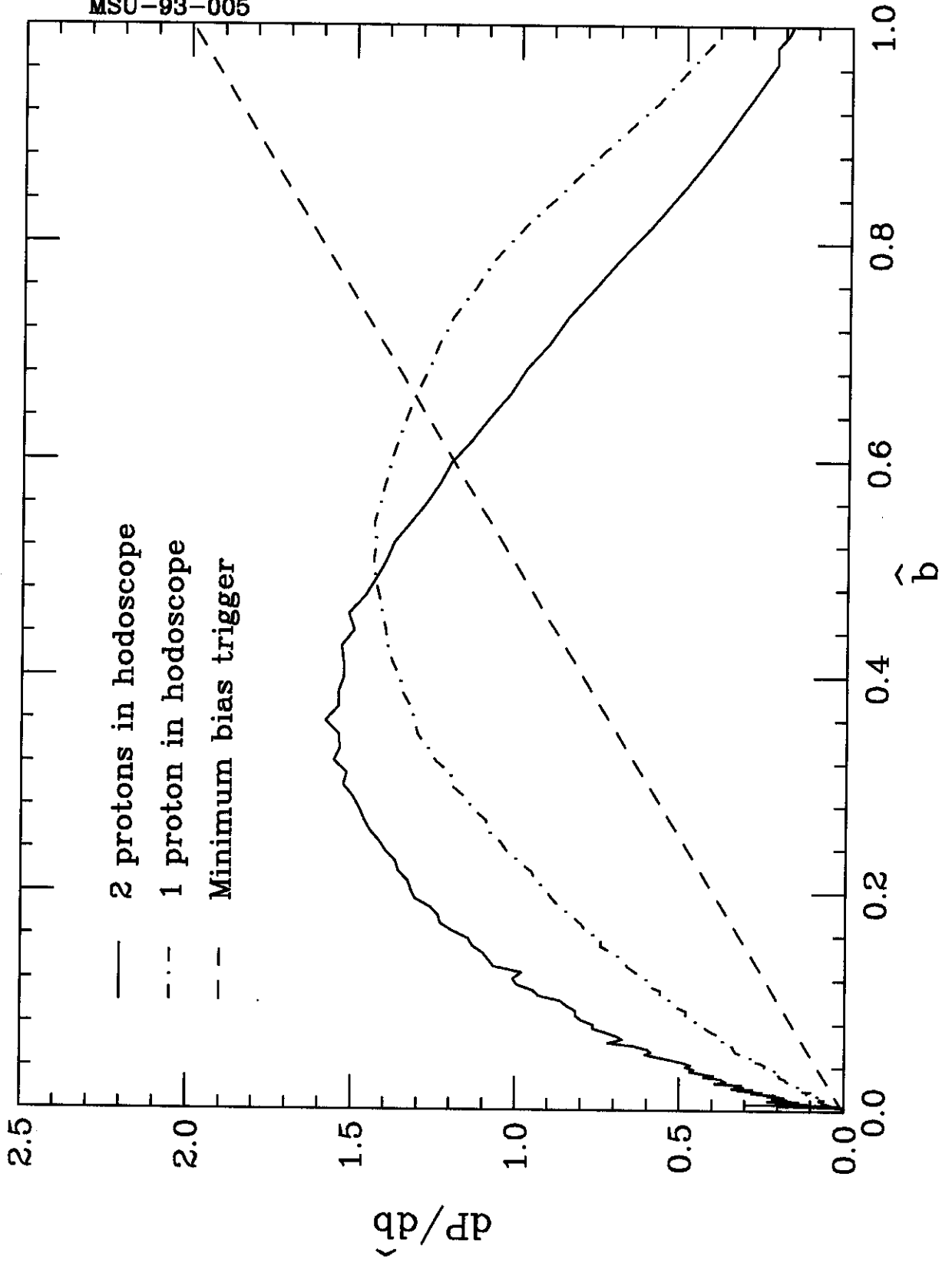
$^{36}\text{Ar} + ^{45}\text{Sc}; E/A = 80\text{MeV}$

MSU-93-004



$^{36}\text{Ar} + ^{45}\text{Sc}; E/A=80\text{MeV}$

MSU-93-005



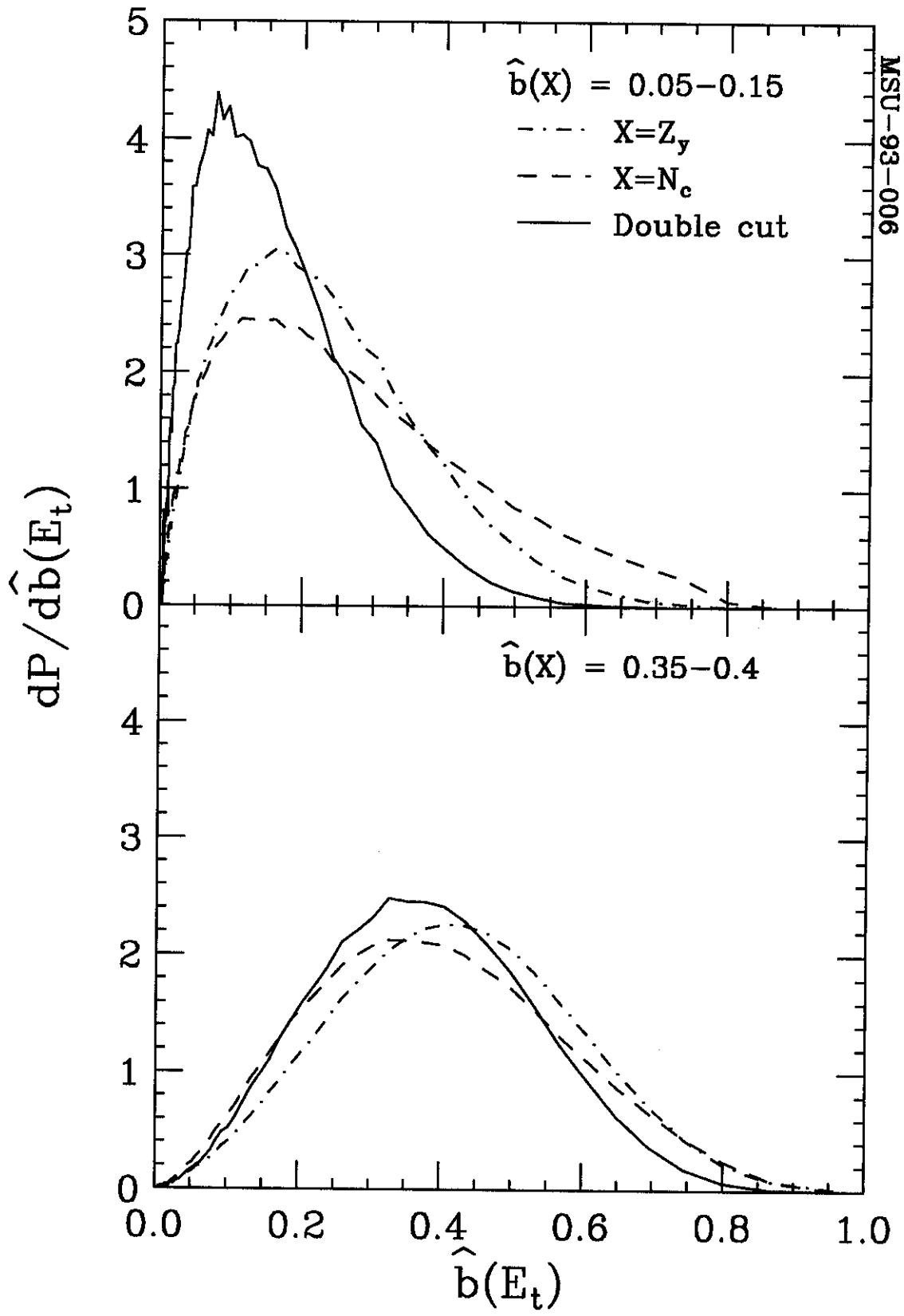


Fig 5

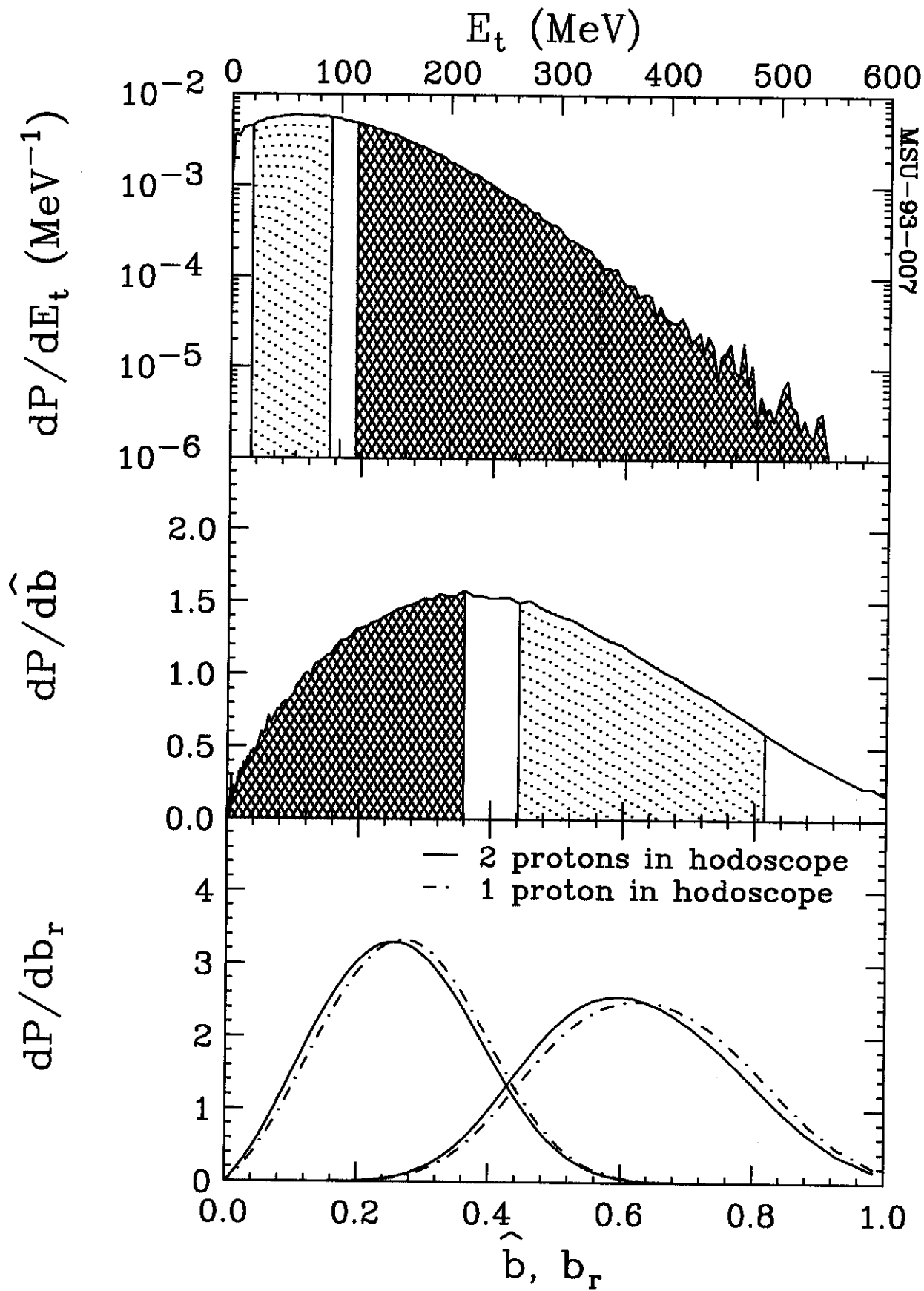
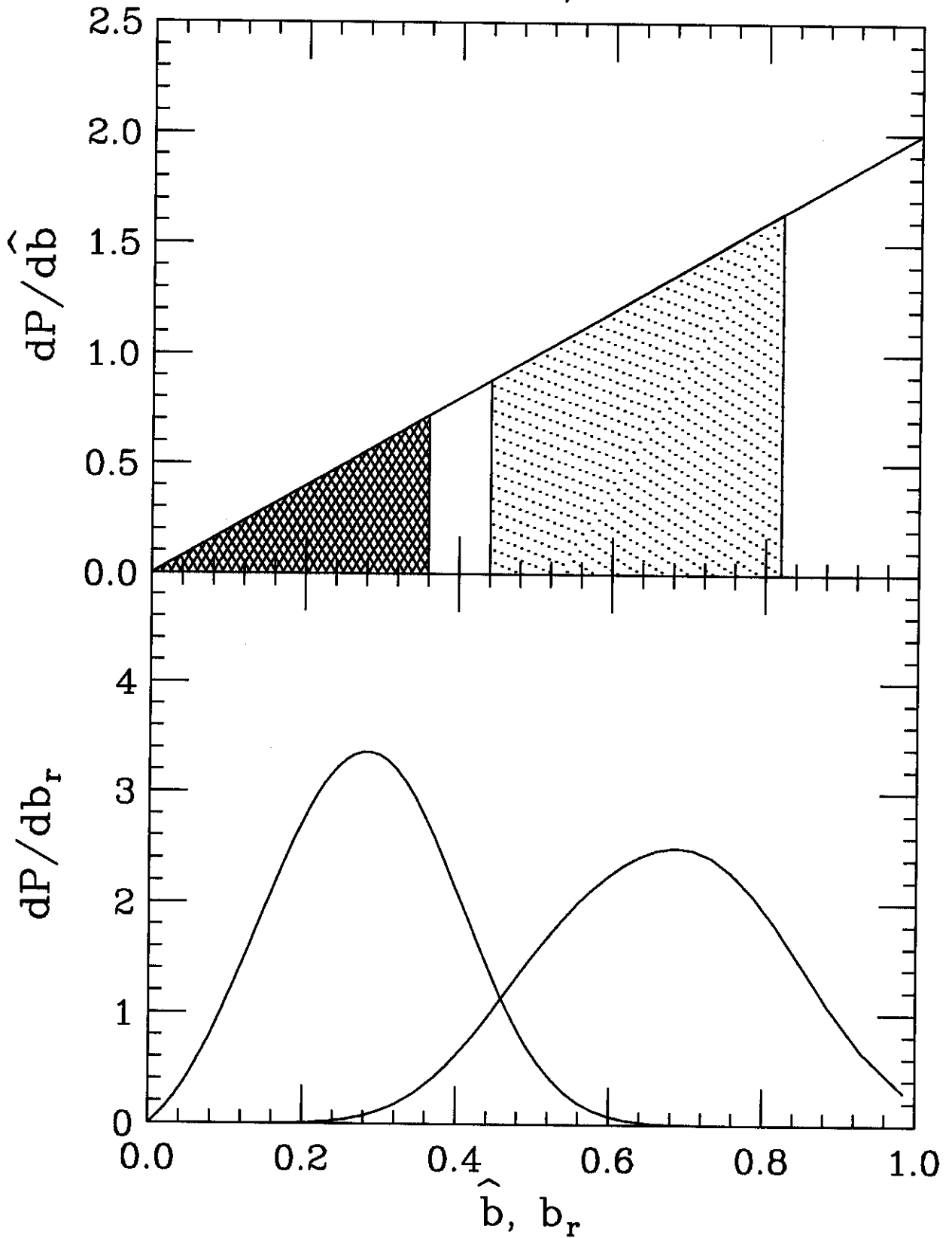


fig 6

$^{36}\text{Ar} + ^{45}\text{Sc}; E/A = 80\text{MeV}$



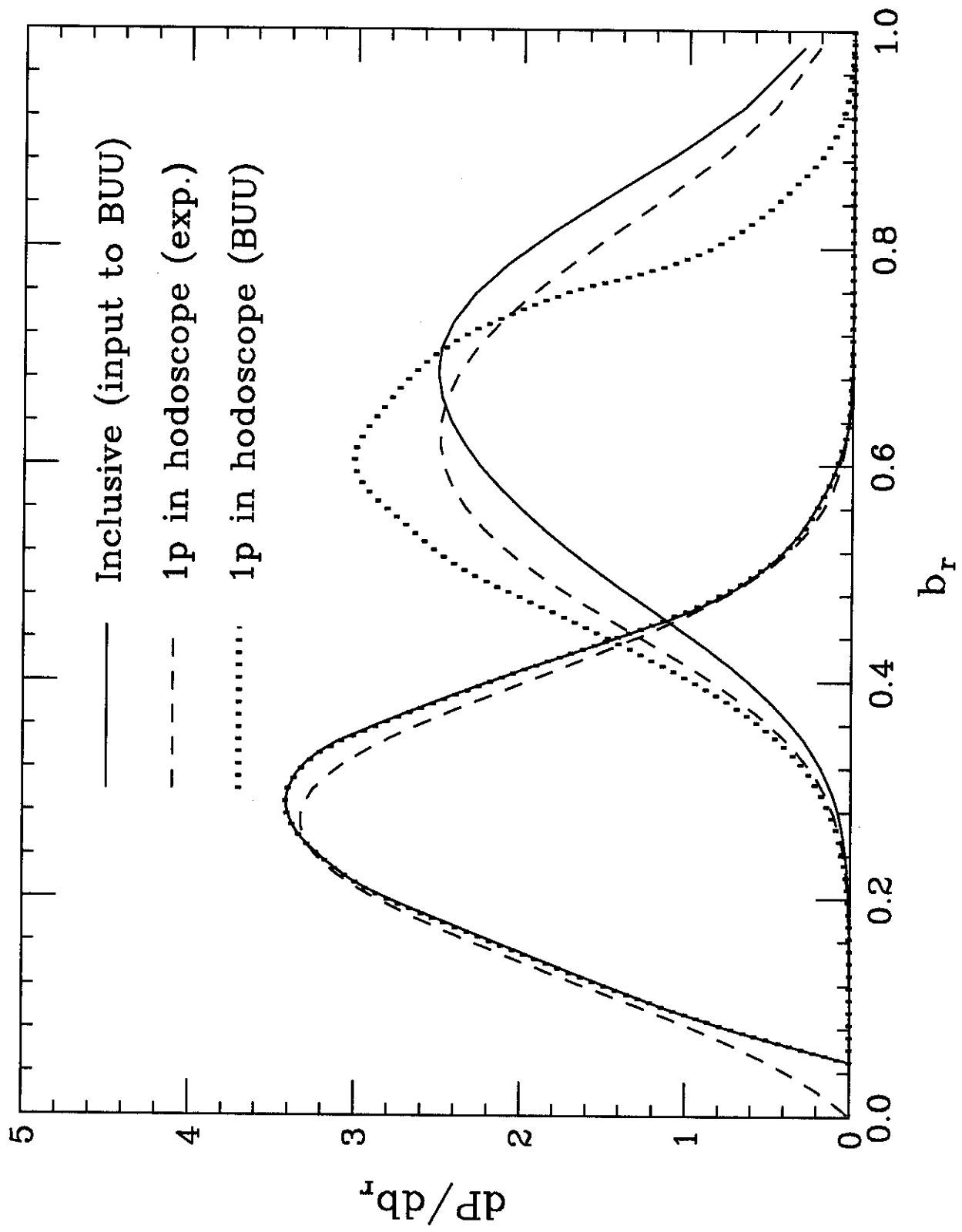
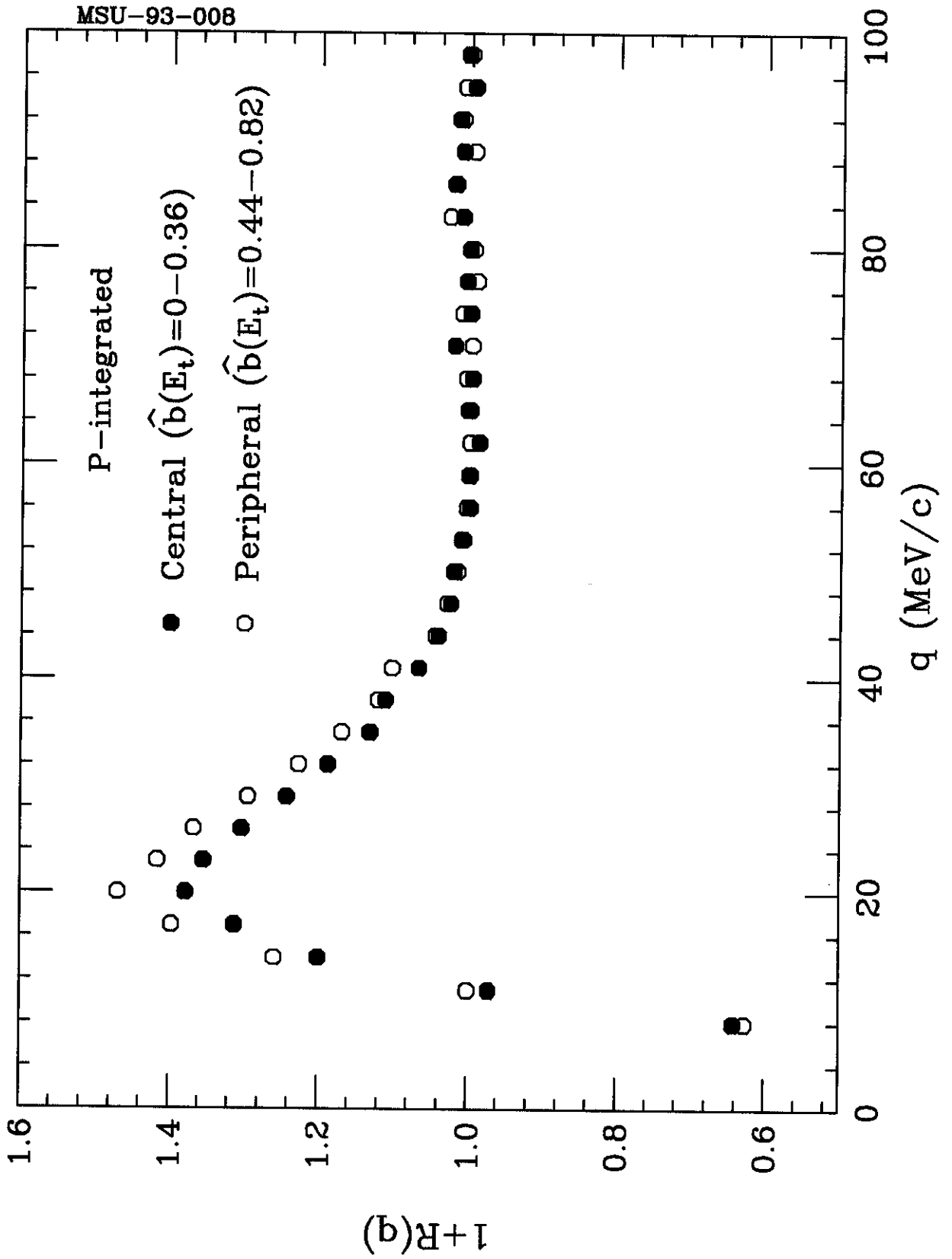
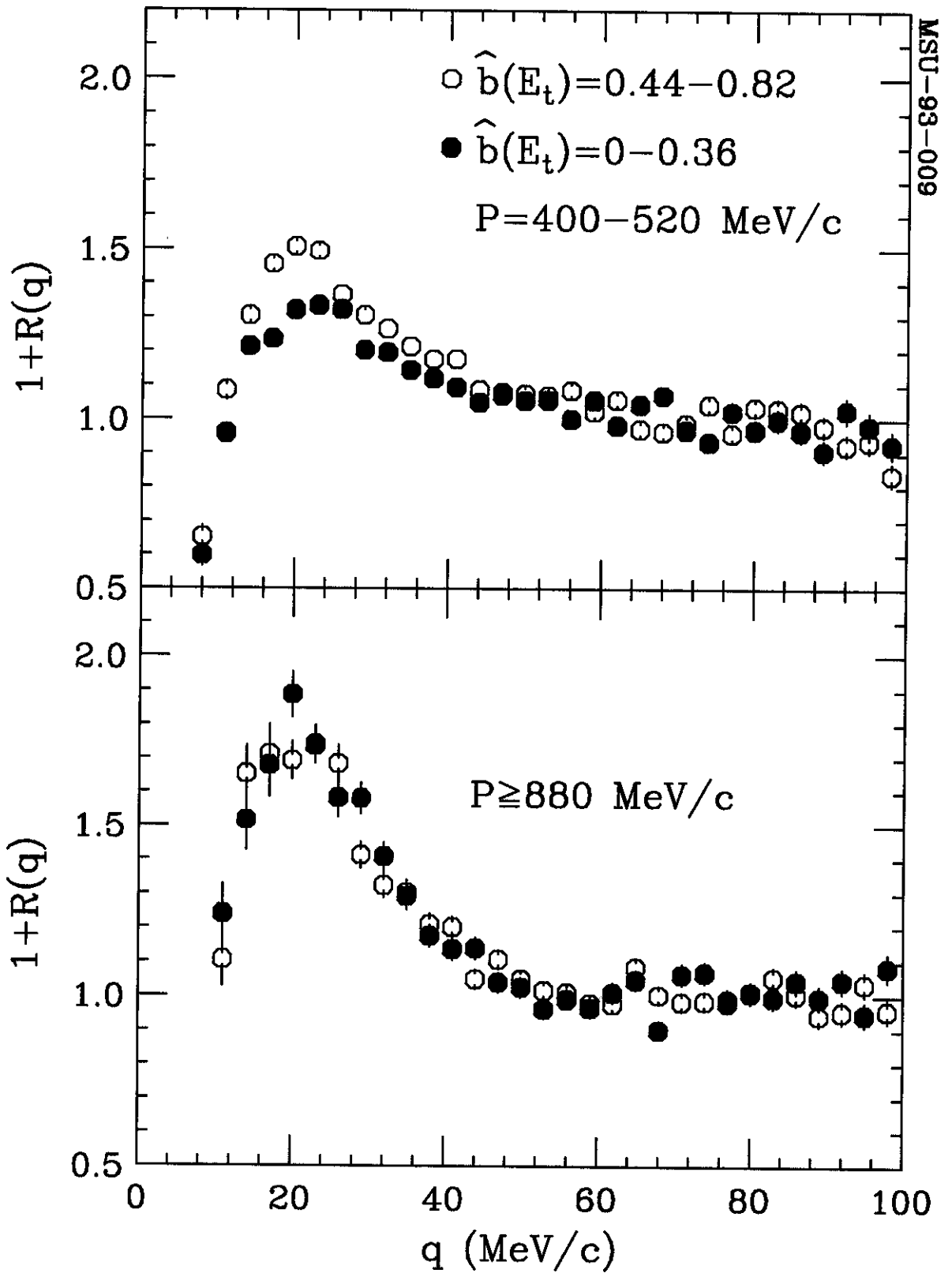


fig 8

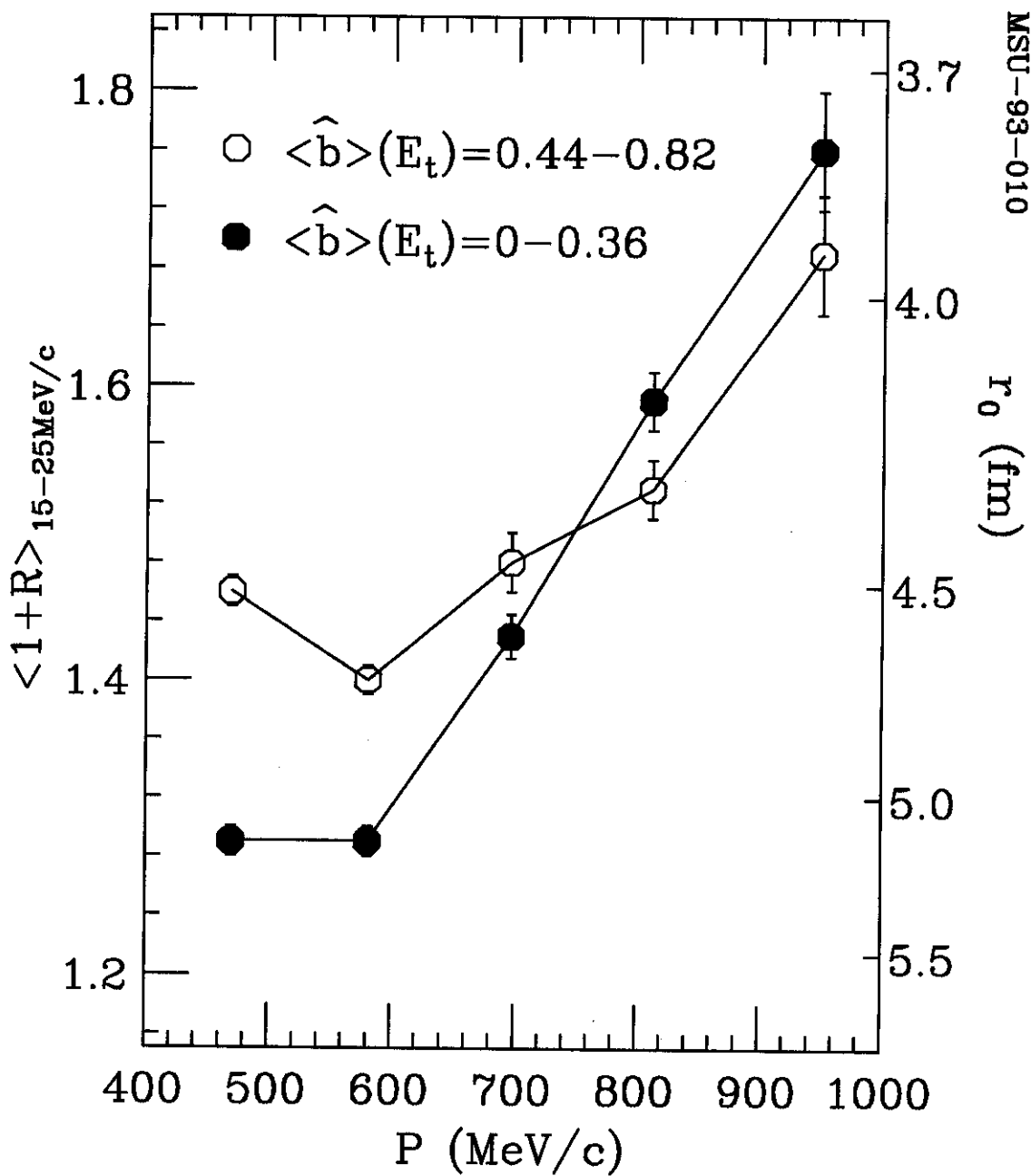
$^{36}\text{Ar} + ^{45}\text{Sc}; E/A=80\text{MeV}; \langle \theta_{\text{lab}} \rangle = 38^\circ$



$^{36}\text{Ar} + ^{45}\text{Sc}; E/A = 80\text{MeV}; \langle \theta_{\text{lab}} \rangle = 38^\circ$



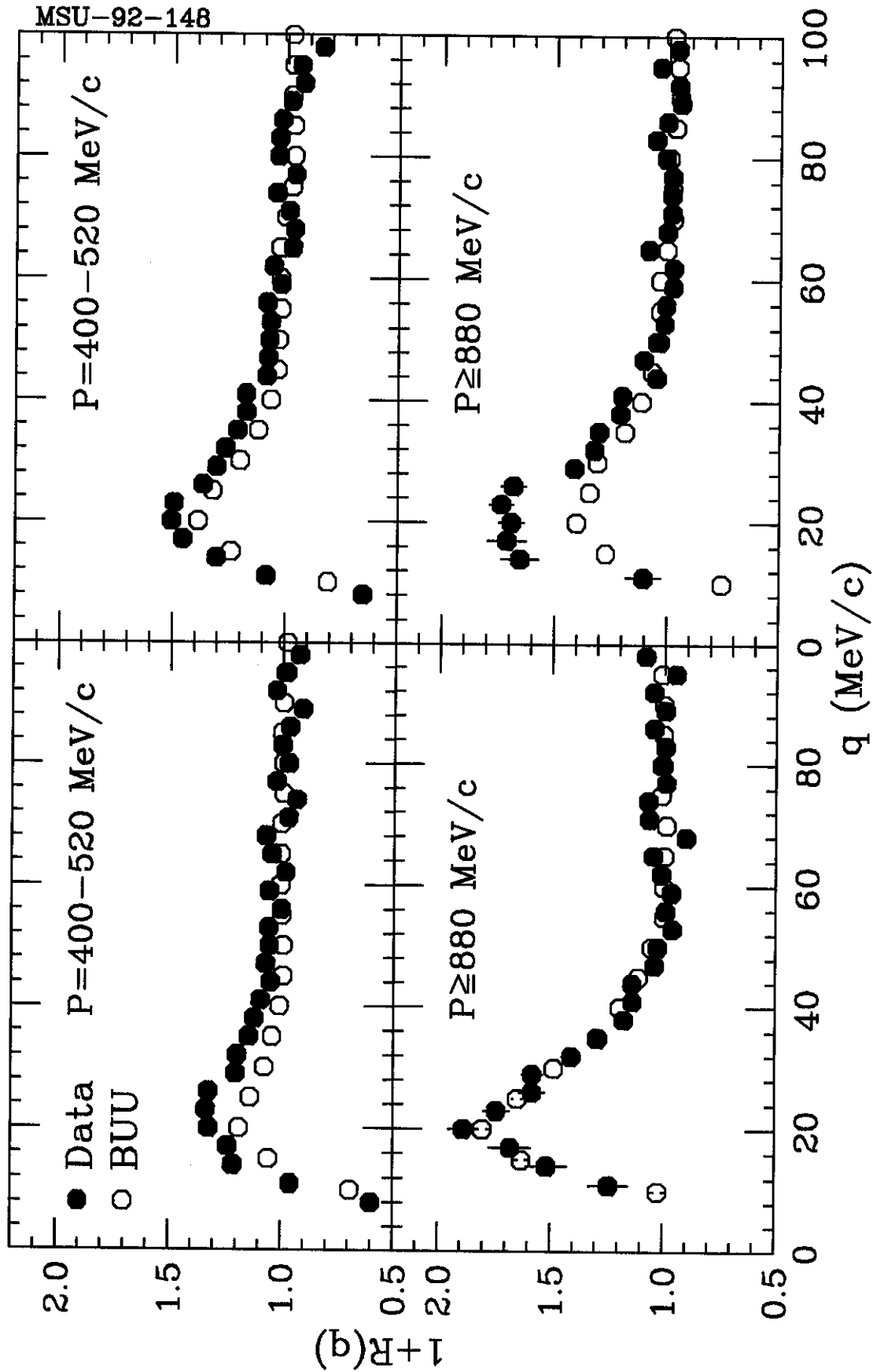
$^{36}\text{Ar} + ^{45}\text{Sc}; E/A=80\text{MeV}; \langle\theta_{\text{lab}}\rangle=38^\circ$



$^{36}\text{Ar} + ^{45}\text{Sc}; E/A = 80 \text{ MeV}; < \theta_{\text{lab}} > = 38^\circ$

$\hat{b}(E_t) = 0 - 0.36$

$\hat{b}(E_t) = 0.44 - 0.82$



$^{36}\text{Ar} + ^{45}\text{Sc}; E/A = 80\text{MeV}; \langle \theta_{\text{lab}} \rangle = 38^\circ$

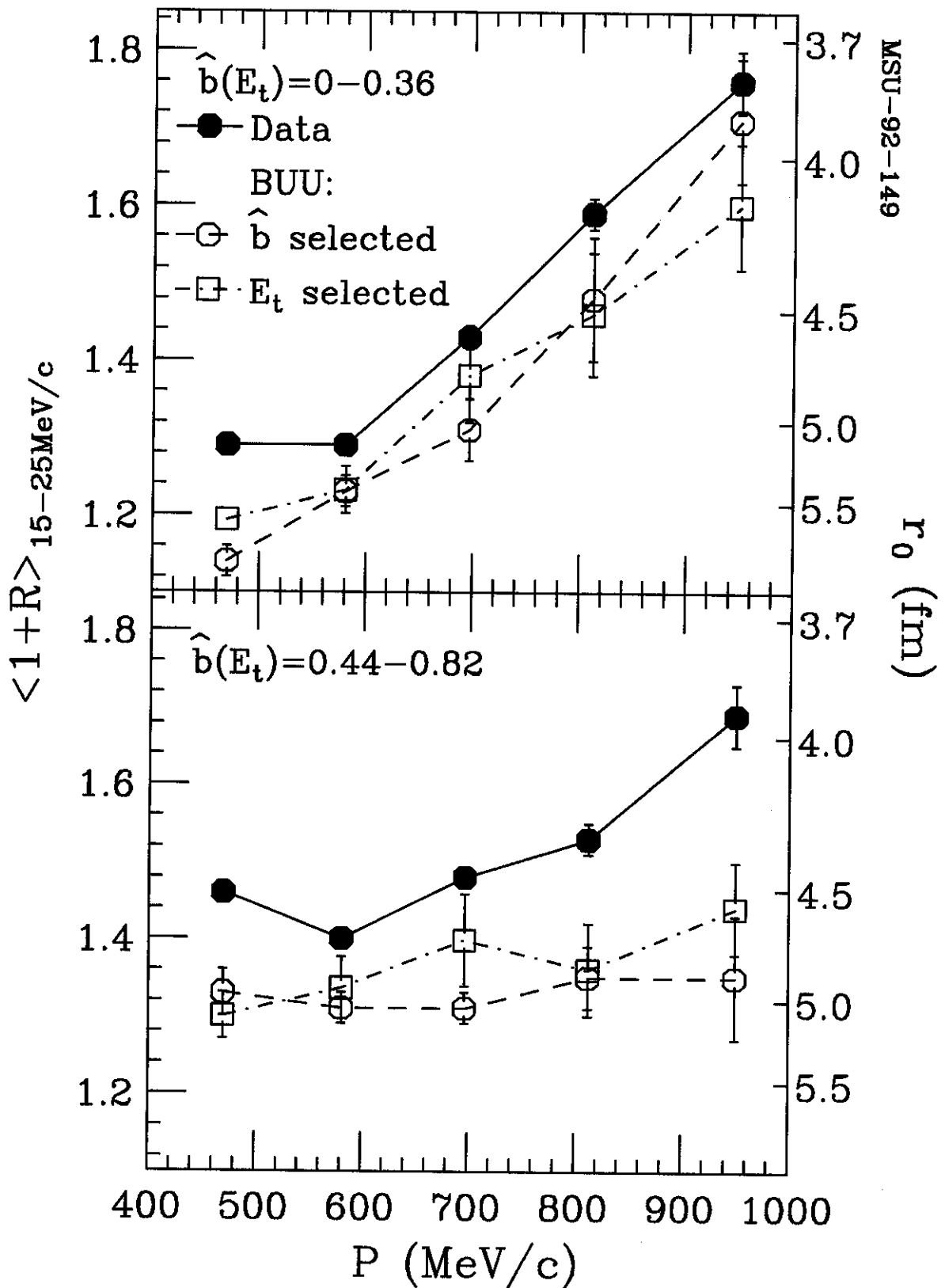


fig 13